Available online at www.sciencedirect.com

jmr&t Journal of Materials Research and Technology

journal homepage: www.elsevier.com/locate/jmrt

Original Article

Effect of roasting pretreatment on micro-nanobubble-assisted flotation of spent lithium-ion batteries

Sabereh Nazari [a], Jinlong Li [a], Hamid Khoshdast [b,c], Jiahao Li [a], Cuiling Ye [a], Yaqun He [a,**], Ahmad Hassanzadeh [d,e,*]

[a] School of Chemical Engineering and Technology, China University of Mining and Technology, Xuzhou, 221116 Jiangsu, China

[b] Department of Mining Engineering, Higher Education Complex of Zarand, 7761156391 Zarand, Iran

[c] Mineral Industries Research Center, Shahid Bahonar Univeristy of Kerman, 76169133 Kerman, Iran

[d] Department of Geoscience and Petroleum, Faculty of Engineering, Norwegian University of Science and Technology, Trondheim, Norway

[e] Maelgwyn Mineral Services Ltd, Ty Maelgwyn, 1A Gower Road, Cathays, Cardiff, CF24 4PA, United Kingdom

ARTICLE INFO

Article history:
Received 28 January 2023
Accepted 18 March 2023
Available online 24 March 2023

Keywords:
Spent lithium-ion batteries
Cathode and anode materials
Roasting process
Nano-micro bubbles
Roasting-assisted flotation

ABSTRACT

In this research study, a novel process of roasting-assisted flotation was developed for the separation of spent vehicle lithium-ion batteries (LIBs) in the presence of micro-nanobubbles (MNBs). For this purpose, roasting technology along with MNBs was applied to overcome the challenge of poor efficiency of electrode active materials flotation. The roasting properties (temperature: 300–500 °C and time: 1 h) and corresponding surface alterations of the electrode active materials (zeta potential, contact angle, and X-ray photoelectron spectroscopy (XPS)) were analyzed to explore the surface properties of roasting materials in the presence of MNBs. MNB-assisted flotation was employed to effectively separate the cathode active materials (CMs) from anode active materials (AMs). Results showed that the efficiency of electrode materials flotation without the roasting process was low due to the existence of residual organic binders and electrolytes. Scanning electron microscope (SEM) coupled with energy dispersive spectroscopy (EDS), XPS and zeta potential analyses showed that the electrolyte residuals and organic binders were eliminated following roasting at 400 °C for 1 h. After roasting, the zeta potential of the CMs and AMs increased from −55 ± 2 to −26 ± 1 mV and −46 ± 1 to −30 ± 1 mV, respectively. These improvements indicated that CM surfaces were more hydrophilic, while the AM surfaces were more hydrophobic. In the presence of MNBs, contact angle measurements showed the highest and lowest values of 91 ± 1° and 29 ± 1° for the AMs and CMs, respectively at 400 °C. It was found that the flotation performance was improved after the roasting process and in the presence of MNBs and relatively lower reagent consumption

* Corresponding author.
** Corresponding author.
E-mail addresses: yqhe@cumt.edu.cn (Y. He), ahmad.hassanzadeh@ntnu.no (A. Hassanzadeh).
https://doi.org/10.1016/j.jmrt.2023.03.133

(50%) was required to obtain higher recovery. Two-stage flotation processes in the presence of MNBs could further upgrade the grade of CMs from 65 ± 2% to 93 ± 3%.

1. Introduction

According to the Global Battery Alliance, 34 million electric vehicles (EVs) will be sold by 2030, with batteries weighing 200–500 kg based on vehicle type [1]. In this way, battery material demand is expected to grow rapidly, leading to serious issues such as waste management and battery recycling [2,3]. Furthermore, these batteries are expected to have a life period of only 10–15 years [4,5]. Thus, recycling spent LIBs is beneficial both for preserving resources and protecting the environment. Pyrometallurgy, hydrometallurgy, and flotation are the main methods that can be used for recycling high-value metals (e.g., Co, Ni, and Cu) from batteries [6,7]. Moreover, cathode materials (CMs) are promising recycling targets for hydrometallurgical and pyrometallurgical processes due to their valuable metal content (mainly Mn, Li, Ni, and Co). With respect to the pyrometallurgical processes, it is hard to separate slags from metals, and mixed powders (CMs and AMs-graphite powders) are difficult to process [3,7].

On the other side, flotation can be potentially used to separate electrode materials based on their wettability differences [8,9]. Since anode materials (AMs) and CMs have obvious and relatively significant differences in wettability [10–12], flotation can be considered an effective way to separate them. However, it has been addressed that spent electrode materials exhibit poor flotation properties due to their organic coatings and damaged/changed surfaces [13,14]. Therefore, it is necessary to modify electrode materials' surfaces before the flotation process to improve their flotation behavior. To date, some technologies have been used to remove organic residues from spent electrode materials [3,14–16]. The varied techniques include conventional grinding [4], cryogenic grinding [17], ultra-high shear forces [18,19] and thermal treatments [3,15,20]. An investigation conducted by Yu et al. on the flotation of spent LIBs, showed that 97.1% $LiCoO_2$ was obtained from mechanical grinding but only 49.3% was recovered [4,14]. In another investigation, it was reported that the grade of concentrate and the recovery of CMs were improved by cryogenic grinding pretreatment at 196 °C [17]. Based on a high-shear blender with ultrahigh shear forces, 66% of the $LiCoO_2$ in the concentrate of the flotation process was recovered, and the grade of the concentrate was 90% [18]. As a result of its efficiency and simplicity of upscale, roasting and pyrolysis were examined as thermal treatment methods. It was shown that CMs could be recovered between 80 and 98%, and AMs could be recovered about 95–98% through the froth flotation processes [3,15,21,22]. In a study by Wang et al., it was found that most of the organic outer layer was removed from the electrode surface via roasting at 450 °C. As a result of roasting treatment, 97.66% of the electrode active materials were recovered [15]. Following pyrolysis pretreatment to remove organic binders, Zhang et al. efficiently used flotation technology for purifying CMs from AMs with CMs recovery and grade of 83.75% and 94.72%, respectively [19]. Vanderbruggen et al. showed that LMO recovery was significantly improved after pyrolysis-mechanical attrition pretreatment from 70% to 85%, while graphite recovery was not affected [23].

Furthermore, MNB-assisted flotation has been widely used for many particle types recently, including coal [24], muscovite [25], quartz [26–28], scheelite [29], phosphate [30], graphite [31] and chalcopyrite [32]. Increasing the hydrophobicity of minerals and reducing reagent consumption have all been proven by MNBs to improve the efficiency of flotation processes [33–36]. Ultrafine bubbles nucleate without collision at the surfaces of hydrophobic particles in flotation of ultrafine and fine particles. In this way, the flotation performance can be improved since common/conventional air bubbles (CBs) attach easily to them [33,37–39]. Nazari et al. [31] showed that introducing nanobubbles (NBs) enhanced the flotation kinetics rate and recovery of flotation of AMs by 33% and 15%, respectively. Ma et al. [40] studied the physical upgrading of graphite with NBs. They showed that the novel process can produce a concentrate with 94.82% carbon grade and 97.89% recovery from an open circuit of one rougher and two cleaner flotation stages. Zhang et al. [41] reported that the NBs had a good hydrophobic agglomeration effect on the ultra-fine graphite particles. Furthermore, the flotation kinetic test results showed that the NB-assisted flotation could complete the flotation operation in only 0.5 min, while the traditional flotation needs 0.625 min. A study conducted by Farrokhpay et al. [35] examined fine particle kinetics in the presence of CBs and microbubbles (MBs), and demonstrated that the kinetic rate of quartz flotation rate was higher using MBs due to the increased hydrophobicity [42]. According to Rulyov et al. [26], the formation of coarse clusters of MBs and beads was responsible for the enhanced recovery of column flotation of glass beads. The experiments conducted by Ma et al. [43] revealed that the recovery of coal increased by 10–39% when ultrafine bubbles were present, the concentration of collector and frother was halved, and the consumption of air was reduced. Ahmadi et al. [38] showed that using MNBs improved the flotation recovery of fine particles of chalcopyrite by 16–21%.

Thus, based on the problems of the secondary resource utilization of the spent LIBs, in this research work, roasting/MNBs-assisted flotation was applied for enhancing the flotation performance of electrode active materials. The roasting pretreatment was aided to unwrap the electrode particle surface from residuals of organic binders and electrolytes. The surface cleaning performance of roasting at different temperatures was evaluated using numerous advanced analysis methods. Afterward, the effect of MNBs on the flotation performance of electrode active materials after surface modification was evaluated through an extended experimental program.

2. Materials and methods

2.1. Sample preparation and roasting pretreatment

Spent LIBs from waste vehicle batteries (type 18650, Jiangsu State, China) were used as initial feed to flotation experiments after pretreatments. A 5% NaCl solution was utilized to discharge the batteries which lasted for 48 h. A manual dismantling process was then performed to obtain electrode anodes and cathodes scraps. The main CM and AM components were identified as $LiCoMnNiO_2$ and graphite, respectively. Fig. 1 illustrates the main steps in the preparation and roasting pretreatment of the electrode sample. Roasting tests on electrode materials were conducted under a temperature range of 300–500 °C for 1 h using a muffle furnace (MXG1200-80 model, Shanghai Micro-X Co., China). In each test, electrode materials were placed in corundum boats and then heated in the muffle furnaces. After the roasting process, the samples were crushed using an impact crusher for 30 s and then sieved by a 45 μm screen to obtain AMs, CMs, and mixed materials. Then, the products were used for the experiments.

2.2. Sample characterization and identification

A laser particle size analyzer (LPSA, GSL-1000 model, Liaoning Co., China) was applied to measure the particle size distribution of the comminution product. For this purpose, five consecutive measurements were performed for each sample and the average value was reported. Through the use of X-ray photoelectron spectroscopy (XPS, 250Xi model, Thermofisher Escable, USA), transmission electron microscopy (TEM, G2 F20 model, FEI Tecnai, USA), and scanning electron microscopy (SEM, 250 model, FEI Quanta, USA) combined with energy dispersive spectroscopy (EDS, Bruker Quantax 400-10, Germany), the roasting characteristics of CMs and AMs were analyzed in detail. The phases and particle properties were analyzed using the X-ray diffraction method (XRD, Bruker D8 Advance, Germany) under Cu-Ka radiation. The key settings of XRD measurement were fixed at a current of 30 mA, accelerating voltage of 35 keV, and scanning range and speed of 3–75° and 0.5 s/step, respectively.

The surface properties of electrode material, before and after roasting pretreatment, were characterized by advanced analysis techniques. In this respect, the zeta potential of electrode materials in the presence and absence MNBs were measured using a potentiometric analyzer (ZetaPALS, Brookhaven, United States). Automatic runs for each tested sample were carried out five times continuously. The average and standard division for each measured sample was calculated. Contact angles of initial and pre-treated electrode materials were also measured to determine the wettability of the surface of electrode materials (JC2000D1 model, Zhongchen Co., China). For each measurement, the well-known sessile drop approach was applied and drops of deionized water were put in six different positions at the surface of samples and the average contact angle values were reported [31].

2.3. MNBs generation and flotation process

2.3.1. MNBs generation

The MNBs were produced using a bubble generator (Xiazhichun Company, Kunming, China). The generator mixes air with water using a pump/venturi tube loop and releases a uniform emulsion-like bubbly stream through a tight nozzle. For flotation experiments, MNBs were produced by circulating 5 L of ultrapure deionized water through the generator. The conditions of MNBs production were controlled by adjusting the aeration rates (0–2 L/min) and preparation time (1–10 min). After the water was pumped into the inlet pipe, MBs and NBs were formed in the outlet as a white mixture of gas and liquid.

The appearance properties of MBs in the solution were investigated using focused beam reflectance measurement (FBRM, G400 model, Mettler-Toledo Co., USA) and obtained images were analyzed via the Mettler-Toledo ParticleView V19 system. For this purpose, the bubbly stream flowed through the FBRM probe window directly placed into the aqueous dispersion at a given angle and images were taken dynamically. It is worth noting that during the imaging of MBs, due to the instability of MBs, FBRM was used for real-time monitoring when the bubble generator was running [44]. In the case of NBs, the appearance properties were recorded using a dynamic light scattering apparatus (DLS, Omni model, Brookhaven, USA), but with completely different methodology than that for the MBs. After the preparation of the solution, the aqueous solution was allowed to stand for 5 min to disappear all MBs, and then a small amount of the solution was taken for testing. This was performed to reduce the impact of the presence of MBs on the accuracy of NBs measurements. Detailed information regarding the operating conditions is available in our previous works [31,44]. To determine optimum conditions for MNBs generation, different settings, i.e. airflow rate of 0.5–2 L/min and preparation time of 1–10 min, were

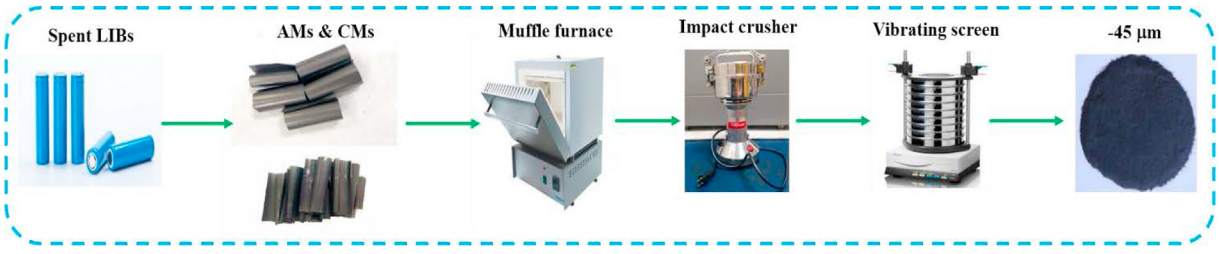

Fig. 1 – Roasting process and sample preparation of electrode active materials.

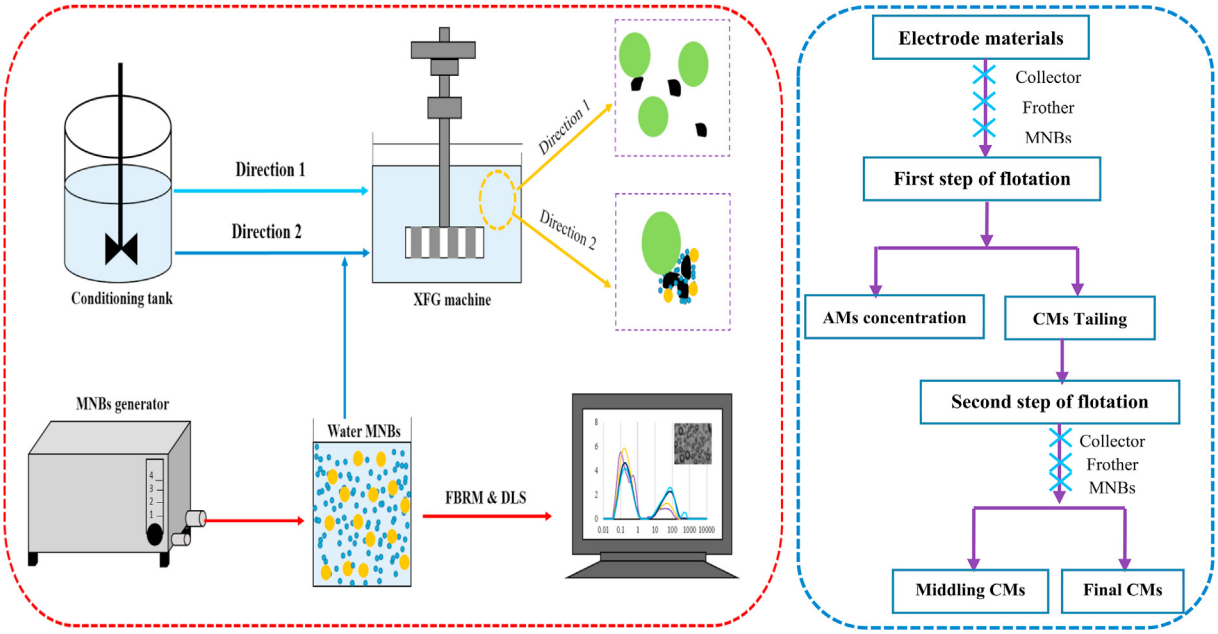

Fig. 2 – Schematic route of the roasting pretreatment followed by the NMB flotation.

examined for the generator and finally, for all flotation experiments, MNBs were prepared at a 0.5 L/min rate during 2 min of operation [31].

2.3.2. *Flotation process*

A laboratory flotation machine (XFD-63 model, Nanchang Jianfeng Co., Chine) was employed for flotation experiments. The fixed conditions during all flotation experiments were impeller speed of 1300 rpm, aeration rate of 120 L/h, N-dodecane (ND) as a collector, and 2-octanol as frother. To avoid any disturbance from external contaminants, all experimental works were performed using ultrapure deionized water with a conductivity of 18.2 MΩ·cm. For every individual flotation test, the appropriate amount of feed material was first weighed, dispersed, and mixed for 3 min in the flotation cell containing 400 mL water. Following that, 300 g/t of ND was added to the cell and conditioned for 3 min. Then, 2-octanol was added in two ways as follows (Fig. 2).

(I) The flotation cell was directly injected with 150 g/t of frother solution without the use of MNBs;
(II) The flotation cell was charged with 75 g/t frother and 1200 cc of MNBs solution at the same time.

Considering 2 min conditioning for frother, the air was then introduced into the flotation cell. The froth floating out of the cell was continuously collected for 3 min. Afterward, the tailing was filtered and dried for the second step of the flotation experiment. The contents of CMs in the flotation products were measured by the XRF. Evaluation of separation efficiency was based on the CMs recovery and grade. The recovery (R, %) was calculated using Eq. (1):

$$R\,(\%) = \frac{Cc}{Ff} \times 100 \tag{1}$$

where C, F, c, and *f* represent concentrate mass (g), feed mass (g), concentrate grade (%) and feed grade (%), respectively.

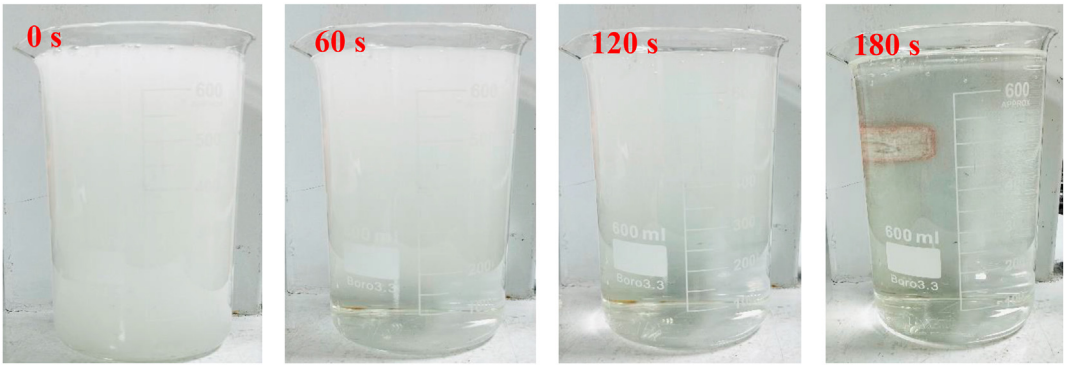

Fig. 3 – A qualitative observation of stability of micro- and nano-bubbles at different time levels.

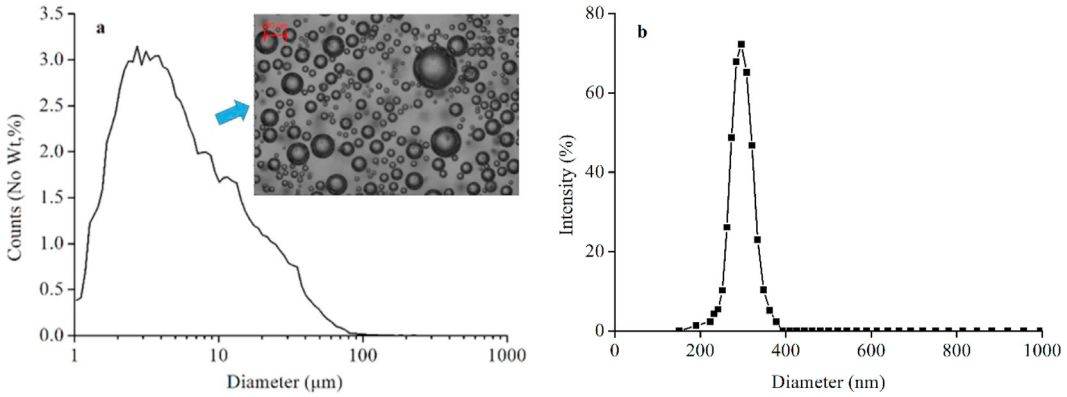

Fig. 4 – The size distribution of bubbles with different scales: a) MBs and b) NBs.

3. Results and discussions

3.1. *Characterization of MNBs*

Fig. 3 illustrates the variation of MNBs water produced by the generator with increasing time. As can be seen from Fig. 3, when the MNBs water was just prepared (0 s), the aqueous solution appeared milky white, with the time increased from 0 s to 180 s, the aqueous solution gradually changed from milky white to clear because the MBs were extremely unstable. As time passed, the MBs gradually floated upwards and ruptured in the water-air interface meaning the solution became clearer and more transparent. At this point only NBs were present in the solution [28,31,44].

Both MBs and NBs play significant roles in the flotation process. However, so far there is no practical way to monitor the MBs and NBs at the same time. The bubbles size distributions of MBs and NBs are shown in Fig. 4a and b, respectively. As seen, the size of MBs was mainly distributed between 1 and 100 μm, where most of them ranged less than 10 μm in size, and the main peak of the bubble size distribution was located around 3–5 μm. However, the size distribution of NBs was narrower than that of the MBs. It was found that, the bubble size distribution of NBs was between 180 and 400 nm where the main peak was situated around 300 nm [31,44].

3.2. *Characterization of feed material*

The particle size distribution curve of feed material, shown in Fig. 5 reveals that the characteristics size (d_{80}) of electrode active material is about 19 μm. The mineral composition of raw electrode material measured using XRD is shown in Fig. 6. The XRD pattern indicates that graphite, the raw anode material, appears at 26.57 and 44.39° while lithium nickel cobalt manganese oxide, the raw cathode material, appears at 18.69, 36.72, 44.39, 48.61, 54.69 and 64.55°.

3.3. *Effect of roasting pretreatment*

3.3.1. *Surface morphology of AMs and CMs*

As shown in Fig. 7a and b, TEM and SEM-EDS analyses were employed to characterize the morphology of the electrode material surface after the crushing and roasting stages. According to Fig. 7, organic binders present at the spent electrode

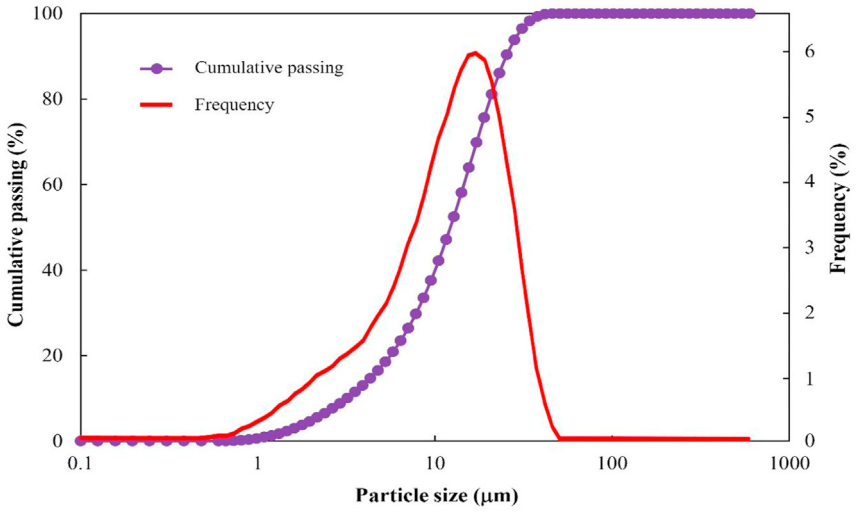

Fig. 5 – Particle size distribution of the feed material.

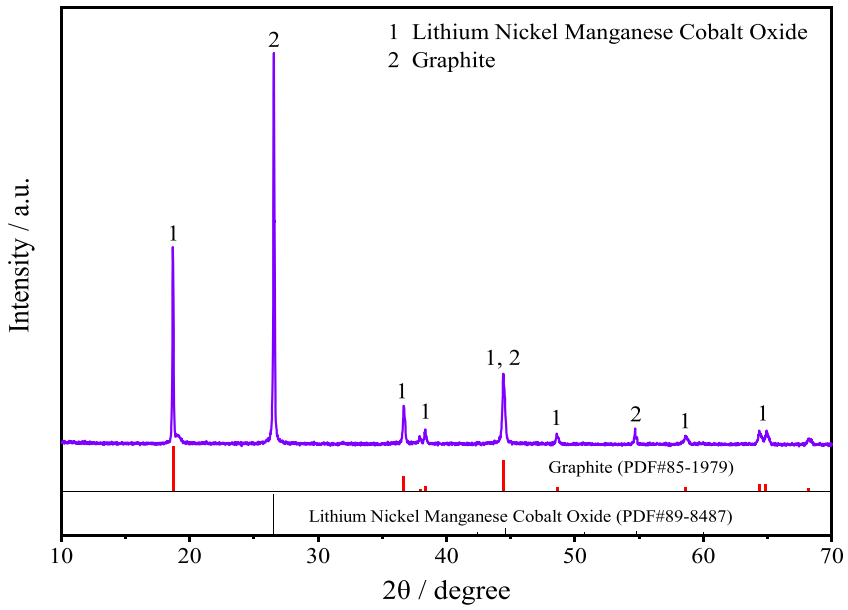

Fig. 6 – The XRD patterns for electrode active materials.

material surface can roughen the surface of electrode particles, which can potentially decrease flotation efficiency. Zhang et al. indicated that the organic binders on the surface of CMs and AMs were Polyvinylidene fluoride (PVDF) and Styrenebutadiene rubber (SBR), respectively [3]. This was addressed in the literature as one of the primary reasons for poor adhesion of graphite to air bubbles [3,16,17,45].

The surface of electrode active materials after roasting at 400 °C for 1 h is given in Fig. 8. At 400 °C, residual organic binders were removed from spent electrode materials. A further investigation of the F element in the EDS images revealed that there were still residual binders on the surface of the electrode particle, which led to partial hydrophilization of some graphite particles (Fig. 8). During the roasting process, the electrode particles were liberated as can be seen in the SEM images. As seen in Fig. 8, the electrode particle surfaces became smoother after organic binder was removed. As a result of exposing the original surfaces, the flotation process can be anticipated more favorably.

3.3.2. *Chemical states of AMs and CMs*

The influence of roasting temperature on the surface chemical properties of CMs and AMs before and after the roasting process was assessed using the XPS technique and the results are shown in Figs. 9 and 10, and Tables 1 and 2. According to the XPS spectrum of CMs and AMs shown in Figs. 9 and 10, the main peak at around 284.25 eV is due to carbon black additive for CMs but from graphite for AMs. The $-(CH_2CF_2)-$n peaks at 286.05 and 290.85 eV attribute to PVDF. The peak at 284.80 eV is from C–C/C–H corresponding to SBR and indicates that there still present some organic binder residuals at the surface of electrode particles. The O–C–O, C═O, and O–C═O functional groups related to ester electrolytes have given peaks at 287.14, 288.06 and 289.00 eV. These oxygen-containing groups may enhance the hydrophilicity of the electrode particle surface and influence interactions between electrode particles and collector molecules. Therefore, the elimination of residual electrolytes would be a crucial factor to improve the flotation response of AMs and CMs [46,47]. Tables 1 and 2 indicate significant reduction in F, O, and C contents. This may show that the organic film has been significantly removed from the surface of the particle and thus, partially exposed surfaces have been provided. There was a significant reduction in F contents from 13.7% to 6.62%, with a decrease rate of 52%. It was evident that SBR decomposed since the main peak attributed to SBR was drastically reduced. Since the electrolyte was removed, the O–C═O and C-OOR functional groups may be disappeared and the content of C═O was reduced.

3.3.3. *The surface potential of electrode particles*

Fig. 11 illustrates the zeta potentials of spent CMs and AMs at different temperatures. In the absence of MNBs, the ND, CMs and AMs have zeta potentials of -47 ± 1 and -55 ± 2 mV at room temperature (25 °C), which increased at higher temperatures. As the temperature increased, the organic layer at the surface of the particles has been disappeared [14,22]. It can be seen from the variations of zeta potential values that the properties of electrode materials surface may be altered. After the addition of ND, the zeta potentials of the CMs and AMs showed a positive shift in comparison to those in the absence of MNBs and ND. As a result of the addition of ND, the particles became hydrophobic and agglomerated, causing the suspension system to become more unstable. As the temperature increased, the zeta potential in the slurry decreased when MNBs and ND were added to the pulp. The negative charge on the surface of the NBs led to a negative shift in the pulp potential [42,48]. The finer nuclei of gas in the water caused the zeta potential to be smaller, thus facilitating particle agglomeration [29]. Based on these findings, MNBs may result in smaller electrostatic repellence forces for particles corresponding to them, and thereby enhance flotation performance [31,44].

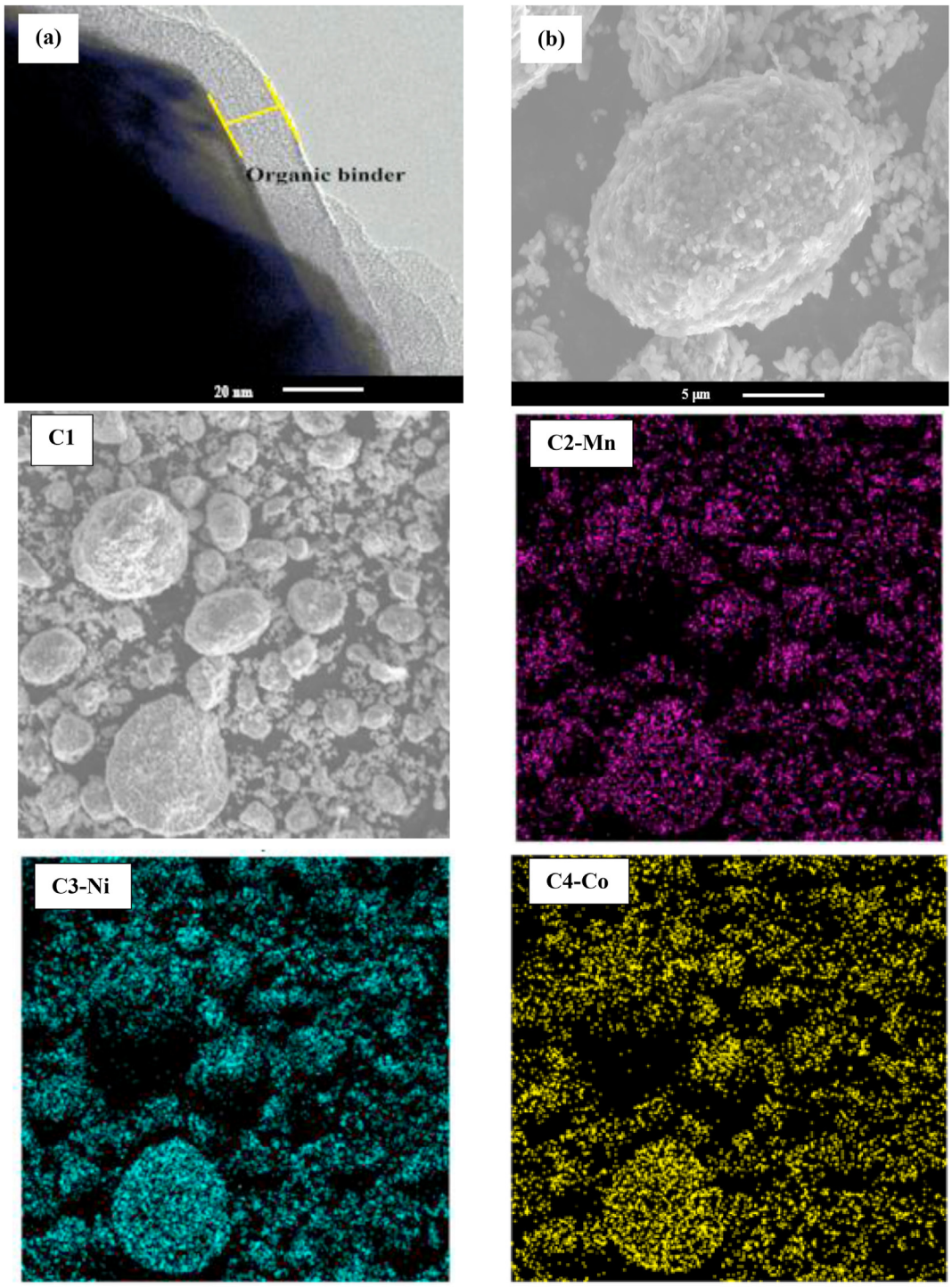

Fig. 7 – (a) TEM, (b, c1-4) SEM-EDS images of CMs after crushing.

3.4. *Mass loss rates*

To reveal the mass loss rate (MLR) during roasting, Eq. (2) was used to compute the MLR (%):

$$MLR\ (\%) = \left(\frac{M_1 - M_0}{M_0}\right) \times 100 \quad (2)$$

where M_0 and M_1 are the mass after and before roasting [49]. Fig. 12 shows the MLRs after roasting for the CMs and AMs in 1 h. MLRs of CMs decreased as the roasting temperature increased. It shows that as the temperature increases, the CMs can easily separate from the surface of foils; however, the results remained similar at 400, 450, and 500 °C. Also, after roasting at 400 °C for an hour, most of the organic outer layer

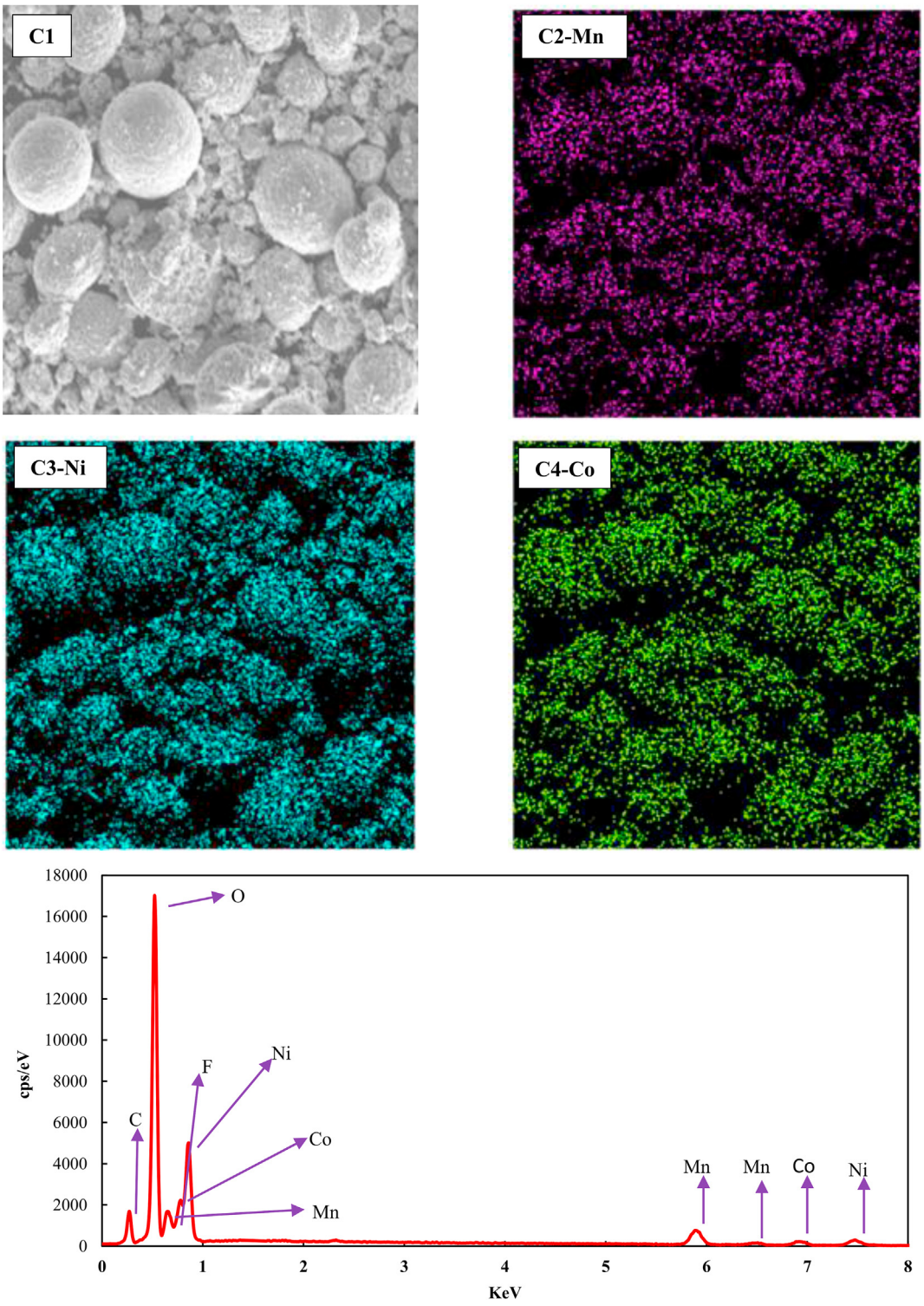

Fig. 8 – SEM-EDS images of CMs after roasting.

was removed. In contrast, the AMs showed an MLR of 56 ± 1% at 400 °C, and it increases with increasing temperature. Also, a roasting temperature of 500 °C resulted in very high MLRs for graphite concentrate. It can be concluded that higher temperatures destroy the graphite structure, and thus MLR increases. Furthermore, high-temperature roasting of graphite leads to the removal of the organic outer layer as well as severe oxidation of the graphite surface that results in a huge amount of oxygen-containing functional groups forming. This caused graphite to become hydrophilic which led to attenuation of the contact angle (Fig. 12) [3,10,15]. It was therefore necessary to reduce the roasting temperature to prevent too

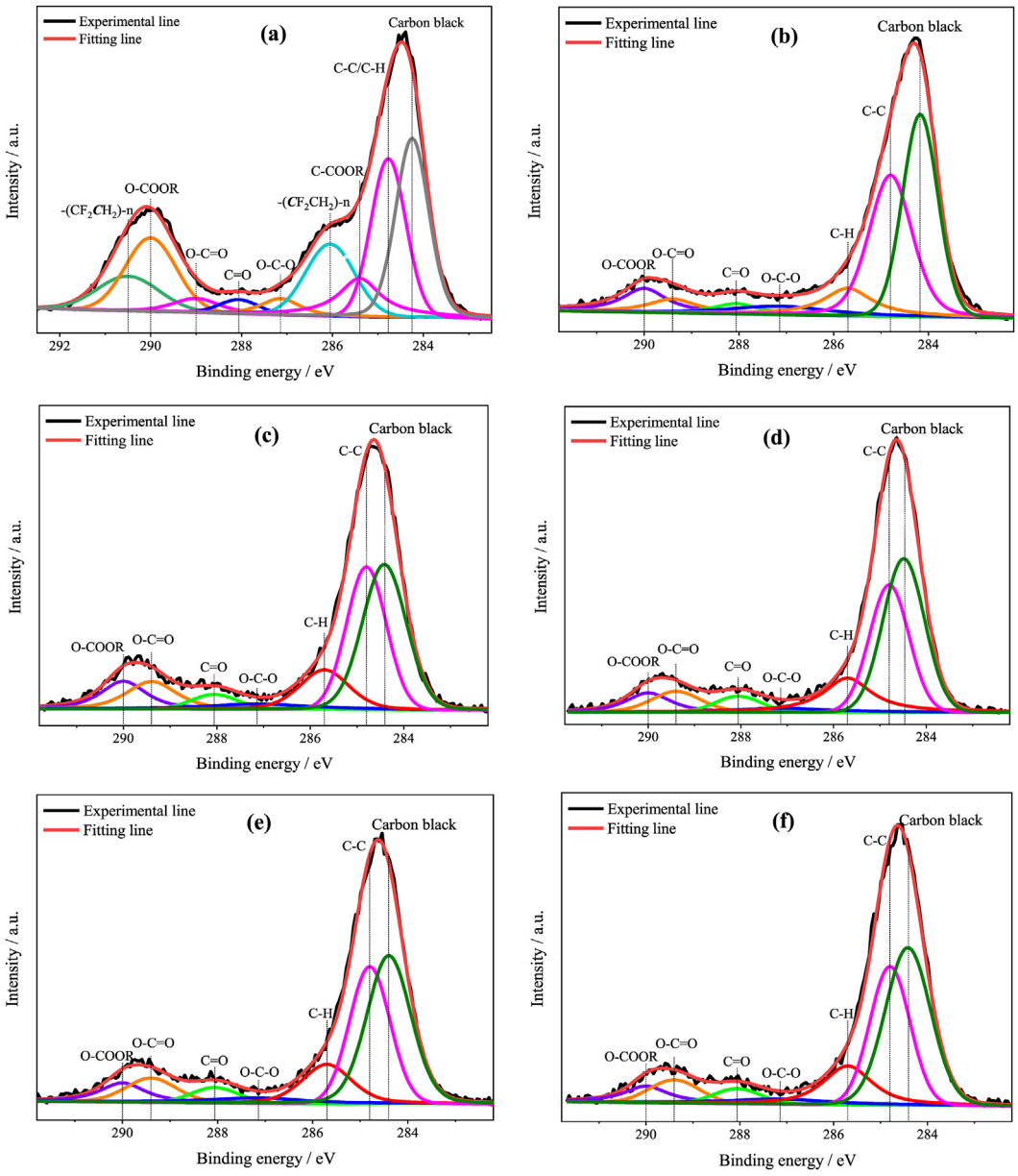

Fig. 9 – C1s XPS spectra of spent and roasted cathode materials: (a) raw CMs, (b) 300 °C, (c) 350 °C, (d) 400 °C, (e) 450 °C, and (f) 500 °C.

much graphite loss. Therefore, roasting at 400 °C for 1 h can improve the properties of electrode materials surface sufficiently to achieve an improved flotation result.

3.4.1. *Contact angle of electrode particles*

To evaluate the wettability of CMs and AMs, the contact angle measurements were carried out. CMs and AMs may represent similar wetting properties due to the presence of residual organic binders, which may interrupt their flotation performance. Therefore, spent electrode materials were exposed to thermal treatment to remove residual electrolytes at temperatures ranging from 300 to 500 °C, and then the contact angles were determined. The effect of the temperature of treatment on the contact angle of CMs and AMs is shown in Fig. 13. As temperatures rise, spent AM's hydrophilicity increases, while spent CMs's hydrophilicity becomes stronger because of removing its organic binders. Thus, the contact angle of CMs gradually decreased, whereas that of AMs increased, which makes flotation an effective method to separate CMs from AMs. Then, contact angle analysis showed that the highest and lowest contact angle of AMs and CMs attained 91 ± 2° and 29 ± 1°, respectively at 400 °C in presence of MNBs. A comparison of the contact angles for concentrate and tailing of flotation processes in the presence and absence of MNBs was shown in Fig. 14. The highest and lowest contact angle of concentrate and tailing were obtained at 400 °C with MNBs, respectively. There is plenty of evidence showing MNBs have a larger microscopic contact angle than CBs [50]. Generally, the presence of MNBs at the surface of particles can upsurge the CBs contact angle and improve the attachment of

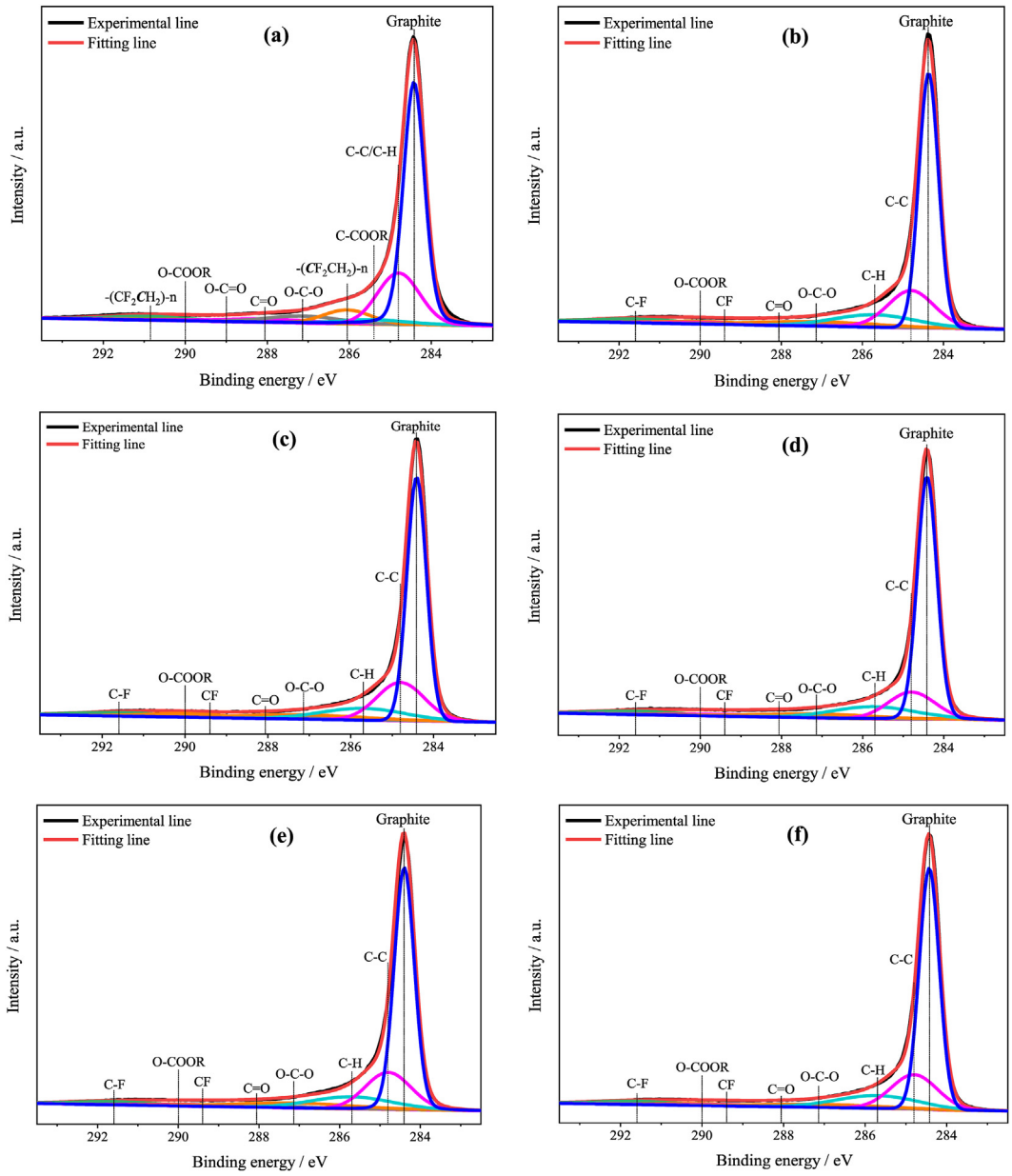

Fig. 10 – C1s XPS spectra of spent and roasted AM: (a) raw AM, (b) 300 °C, (c) 350 °C, (d) 400 °C, (e) 450 °C, and (f) 500 °C.

Table 1 – Chemical states of carbon at the surface of CMs before and after roasting process.

	Components	-(CF_2CH_2)-n	O-COOR	O–C=O	C=O	O–C–O	-(CH_2CF_2)-n	C-COOR	C–C/C–H	Carbon black
Cathode	BE (eV)	290.50	290.00	289.00	288.06	287.14	286.05	285.40	284.80	284.25
	Raw materials At.%	8.28	14.48	3.10	2.17	3.10	13.70	9.31	21.44	24.42

Heating products At. %	Components	O-COOR	CF	C=O	O–C–O	C–H	C–C	Carbon black
	BE (eV)	290.00	289.40	288.06	287.14	285.70	284.80	284.25
	500	5.80	6.01	3.64	3.95	13.18	29.00	38.41
	450	6.43	7.12	3.80	4.28	11.97	29.45	36.95
	400	6.45	6.62	4.16	3.32	14.05	28.80	36.60
	350	8.50	8.85	3.49	4.02	11.37	29.49	34.29
	300	7.85	5.02	3.45	5.65	9.73	32.97	35.32

Table 2 – Chemical states of carbon at the surface of AMs before and after roasting process.

Anode	Components	-(CF_2CH_2)-n	O-COOR	O–C=O	C=O	O–C–O	-(CH_2CF_2)-n	C-COOR	C–C/C–H	Graphite
	BE (eV)	290.85	290.00	289.00	288.06	287.14	286.05	285.40	284.80	284.42
	Raw materials At.%	3.12	1.76	2.95	4.33	5.20	6.68	3.03	22.23	50.69

Heating products At. %	Components	C–F	O-COOR	CF	C=O	O–C–O	C–H	C–C	Graphite
	BE (eV)	291.60	290.00	289.40	288.06	287.14	285.70	284.80	284.42
	500	3.63	1.97	2.65	3.02	4.23	11.79	17.91	54.80
	450	3.17	1.74	2.48	2.64	6.40	10.75	18.27	54.55
	400	3.59	1.75	3.16	3.74	5.46	11.66	14.56	56.07
	350	3.52	3.24	3.07	3.32	5.73	10.63	19.38	51.12
	300	3.64	2.41	1.75	2.41	5.68	10.90	19.28	53.93

particles to CBs that are responsible for directing particles toward the froth phase [25,51]. About the contact angle Wang et al. [52] explained that NBs are adsorbed on the substrate and accompanied by deformation at the same time until a metastable equilibrium state was reached. Then, the air content of froth gradually dissolves and disappears in absence of any external energy (such as agitation, ultra-sonication, etc.). Ishida et al. [53] showed that the macroscopically expected contact angle of NBs was significantly lower than values measured on the liquid side. This abnormally large apparent contact angle of NBs can significantly improve the attachment efficiency of particles and bubbles. Generally, the surface of particles with higher hydrophobic character is a more favorable site for NBs to form, because such particles need less energy required to overcome the adhesion between the surface of particles and water [54,55]. Zhou et al. [29] showed that the efficiency of bubble-particle attachment is significantly influenced by the mass of particles and collision angle. They also revealed that NBs can increase the attachment force by increasing the hydrophobicity of particles as a consequence of improved contact angle. The chief cause behind this phenomenon is that as NBs frost on the surface of particles, the attachment of CBs will enhance following their coalescence with NBs cover over the surface of the particles. Thus, a significantly stable contact angle be appear at the surface of particles [31,56]. Calgaroto et al. [42], for example, showed that the macroscopic contact angle of fine and ultra-fine particles of quartz grew from 18° to 46° in the presence of NBs due to the formation of particle/NBs clusters. A similar result has been also reported by Fan et al. [57] who showed the NBs led to the improvement of the contact angle of anthracite, bituminous coal, and sub-bituminous coal by up to 19°, 24°, and 27°, respectively.

3.5. *MNB-assisted flotation performance of electrode particles*

Results of flotation experiments of the electrode materials pretreated by roasting (400 °C, 1 h) are shown in Fig. 15. The CMs recovery and grade in the tailing product were two evaluation indices in the flotation process. The metals content (Co, Mn, Ni) of raw materials was 65 ± 3%. Results indicate that particles may not be floated without the roasting process and using MNBs. In the first step of flotation of electrode materials, the metal content and recovery at 400 °C in the pulp phase were 74 ± 3% and 78 ± 2%, respectively, demonstrating CMs were not separated from AMs. In the presence of MNBs, the metal content and recovery of electrode active materials were found to be 83 ± 3% and 85 ± 2%, respectively, which were higher than that in the absence of MNBs. The yield of products in the absence and presence of MNBs was 68 ± 3% and 66 ± 2%, respectively. The electrode particle size is fine, and some metal particles are easy to adhere to bubbles and then transfer to the froth product. So, it was concluded that there can be an entertainment of metal contents in the froth product in the absence of MNBs more than the presence of MNBs. According to the results, the flotation experiments were conducted again and a second step of flotation could also improve the grade and recovery of CMs. Thus, in the absence of MNBs, the metals content was up to 84 ± 3% with the yield of 73 ± 3%. The improved recovery and grade of CMs after roasting and with MNBs indicate that hybrid serving of roasting and MNBs can

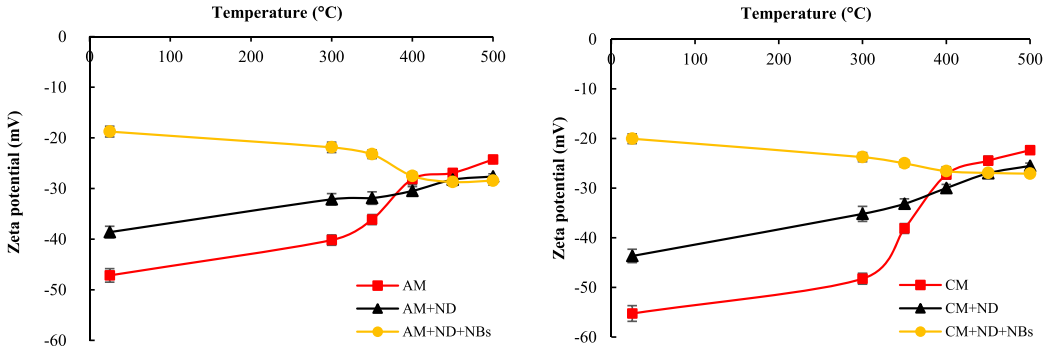

Fig. 11 – Zeta potential variations of AMs and CMs suspensions by ND and MNBs.

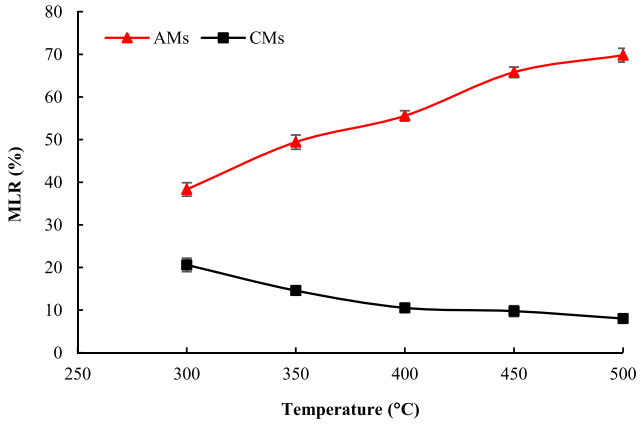

Fig. 12 – Effect of roasting temperature on MLR of electrode materials after 1 h.

play a positive role in the modification of CMs surface and consequently flotation separation, and that significantly less reagent consumption (50%) was necessary to achieve better recovery. Two-step flotation in presence of MNBs could further enhance the grade of CMs to 93 ± 3% with a yield of 81 ± 3%. Thus, some metal particles still remain in the froth product due to fine particle entrainment. So, research on the removal of these particles and optimization of the flotation can be conducted in subsequent studies.

3.6. *Discussions*

The muffle furnace flotation performance of electrode materials was significantly influenced by roasting temperature and roasting time. By roasting pretreatment of spent LIBs, the organic binder can remove from the surface of electrode materials and improve electrode liberation. Also, it can enhance the hydrophilic and/or hydrophobic character of particle surfaces to enhance the efficiency of the flotation process [3,15]. Moreover, a similar phenomenon can be observed between AMs and CMs in which the adsorption capacity of the collector increases by the removal of electrolytes, particularly for AMs. Due to the weak interaction energy between the residual electrolyte and molecules of the collector, the residual electrolyte can hinder the adsorption behavior of the collecting agent. In addition, the electrolytic residuals may dissolve in pulp and changes their chemical and physical characteristics [3,14].

On other hand, while MNBs cover the particles, they make them hydrophobic, which allows CBs to collect them more easily [58]. In addition, MNBs could facilitate particle interaction and increase flotation recovery by acting as "air bridges" [8,59]. In addition, MNBs have been shown to reduce reagent consumption, improve flotation selectivity, and act as secondary collectors [38,60,61]. As compared with CBs, the dissolution rate of NBs may last for a long time from hours up to days, according to Weijs and Lohse [62]. Furthermore, the lower surface tension and significantly higher contact angle of NBs compared to CBs have been demonstrated elsewhere [63,64]. NBs in flotation attach more readily to fine and ultrafine particles because of their specific movement in liquid. The fine particles coated with NBs can thus be attached easily to the CBs and recovered [33,36]. Because the adhesion energy of solid particles/water is smaller than that of water cohesion, ultrafine bubbles tend to preferentially nucleate on hydrophobic particles' surfaces. Moreover, the energy of adhesion declines as the hydrophobicity of the solid surface measured by the contact angle increases. In flotation of fine particles,

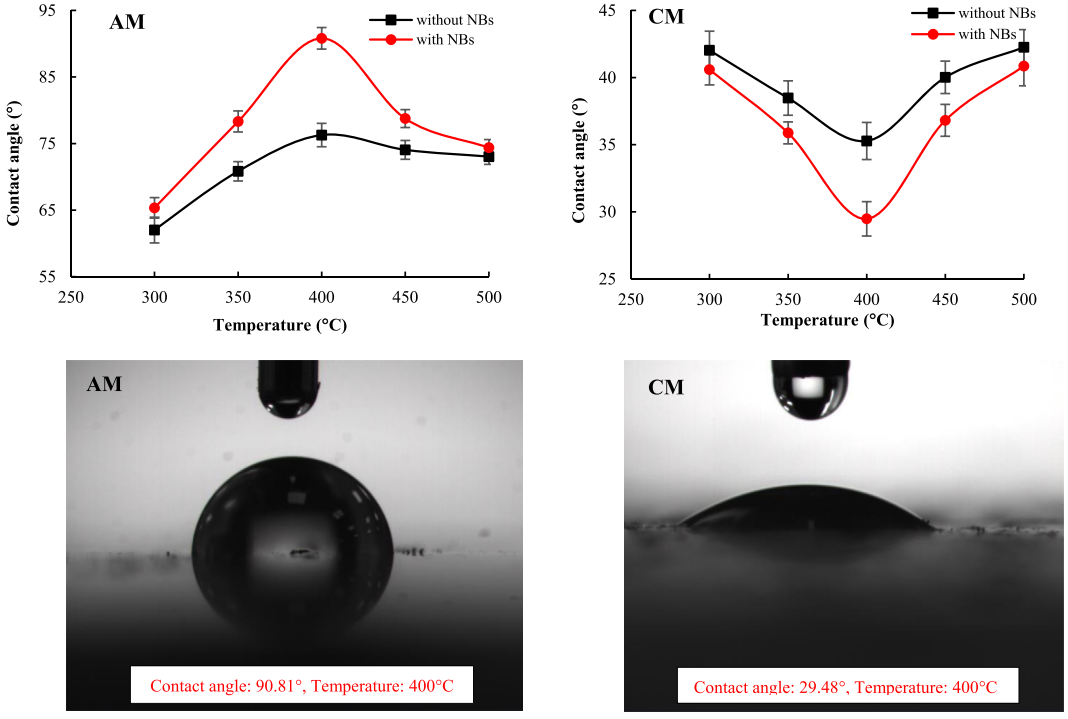

Fig. 13 – Contact angle of AMs and CMs with changing temperature before flotation.

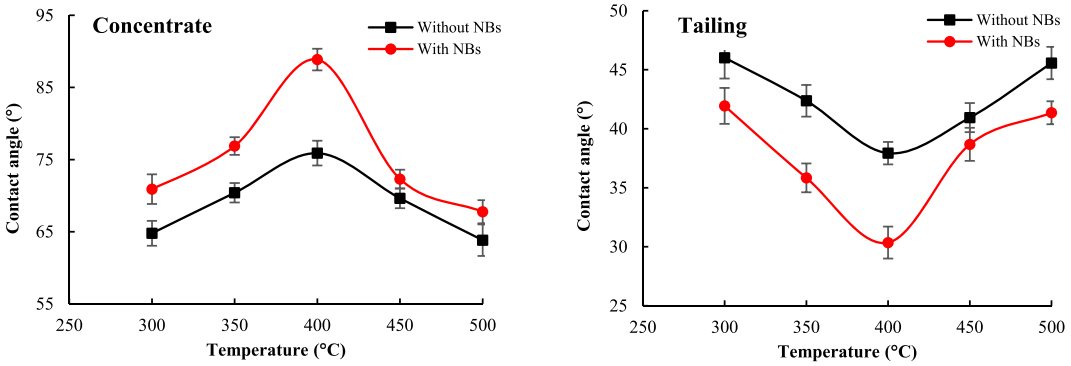

Fig. 14 – Contact angle of concentrate and tailing with changing temperature after flotation.

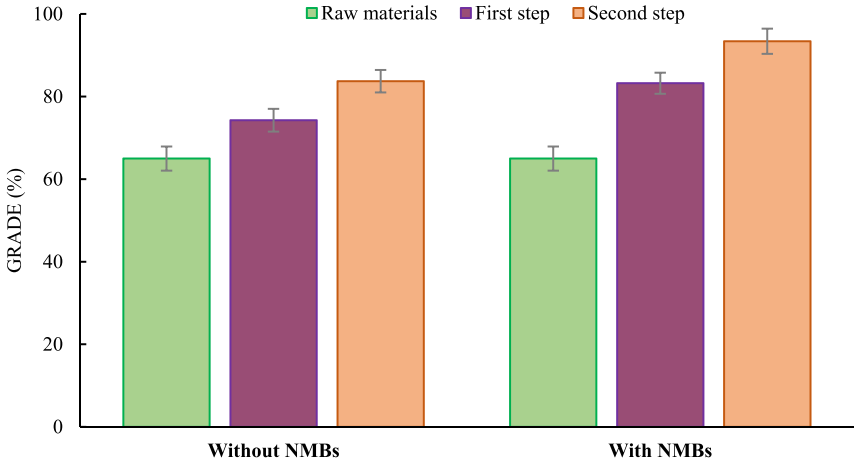

Fig. 15 – Flotation behavior of spent electrode materials after roasting-flotation with and without MNBs.

NBs can nucleate without colliding with ultrafine particles, which is almost often a clincher in the flotation of fine particles [34,39]. The van der Waals forces were strengthened by the use of MNBs which altered the total repulsive force to smaller attractive forces. Furthermore, the competition between the adsorption of MNBs and the collector could stabilize the surface potential, lead to the reduced electrostatic repelling force between particles, and finally, provide conducive conditions for agglomerating particles, which could enhance flotation results [36,54].

4. Conclusions

In this research study, the hybrid effect of roasting and micro-nano-bubbles on the performance of spent electrode materials flotation was investigated through extensive experimental works supported with necessary instrumental analyses. Results indicated that the roasting pretreatment and serving of MNBs improved both the grade and recovery of electrode active materials and reduced the need for reagents. Accordingly, the following conclusions are drawn from this work.

- SEM-EDS indicated that organic binders and electrolyte were removed at the optimal roasting temperature of 400 °C and the surfaces of electrode particles have become smoother after the organic binder was removed.
- XPS analysis showed that there is a significant reduction in F contents from 13.7% to 6.62%, with a decrease rate of 52%.
- As the temperature increased, the zeta potential in the slurry decreased when MNBs and ND were added to the pulp because of the adsorption of OH^- on the surface of particles.
- Contact angle analysis showed that the highest and lowest contact angle of AMs and CMs attained 91 ± 2° and 29 ± 1°, respectively at 400 °C in presence of MNBs.
- After the roasting process, the CMs grade increased from 65 ± 3% to 93 ± 3% in two-stage flotation processes in the presence of MNBs. Further investigations using tap water instead of DI water in flotation experiments could simulate the plant operations for scale-up purposes, which was considered for future test works.

Author contributions

Conceptualization, S.N., Y.H.; methodology, S.N., JL.L., A.H., H.K; investigation, S.N., JL.L., C.Y., JH.L., validation, S.N., JL.L., A.H., H.K; data analysis, S.N., A.H., H.K.; C.Y., JH.L., writing-original draft preparation, S.N., JL.L.; writing-review and

editing, S.N., A.H., H.K., Y.H., JL. L; visualization, A.H., S.N., JL.L., and supervision, Y.H.

Declaration of Competing Interest

The authors declare that they have no known competing financial interests or personal relationships that could have appeared to influence the work reported in this paper.

Acknowledgment

This work was financially supported by the Fundamental Research Funds for the Central Universities (2022QN1072).

REFERENCES

[1] Ellingsen LAW, Singh B, Strømman AH. The size and range effect: lifecycle greenhouse gas emissions of electric vehicles. Environ Res Lett 2016;11:054010. https://doi.org/10.1088/1748-9326/11/5/054010.
[2] Dai Q, Kelly JC, Gaines L, Wang M. Life cycle analysis of lithium-ion batteries for automotive applications. Batteries 2019;5:48. https://doi.org/10.3390/batteries5020048.
[3] Zhang G, He Y, Wang H, Feng Y, Xie W, Zhu X. Application of mechanical crushing combined with pyrolysis-enhanced flotation technology to recover graphite and $LiCoO_2$ from spent lithium-ion batteries. J Clean Prod 2019;231:1418–27. https://doi.org/10.1016/j.jclepro.2019.04.279.
[4] Yu J, He Y, Ge Z, Li H, Xie W, Wang S. A promising physical method for recovery of LiCoO2 and graphite from spent lithium-ion batteries: grinding flotation. Sep Purif Technol 2018;190:45–52. https://doi.org/10.1016/j.seppur.2017.08.049.
[5] New Energy and Industrial Technology Development Organization (Nedo). The Japanese policy and NEDO activity for future mobility. 2017.
[6] Velázquez-Martínez O, Valio J, Santasalo-Aarnio A, Reuter M, Serna-Guerrero R. A critical review of lithium-ion battery recycling processes from a circular economy perspective. Batteries 2019;5:68. https://doi.org/10.3390/batteries5040068.
[7] Niu B, Xiao J, Xu Z. Advances and challenges in anode graphite recycling from spent lithium-ion batteries. J Hazard Mater 2022;439:129678. https://doi.org/10.1016/j.jhazmat.2022.129678.
[8] Nazari S, Shafaei SZ, Gharabaghi M, Ahmadi R, Shahbazi B. Effects of nanobubble and hydrodynamic parameters on coarse quartz flotation. Int J Min Sci Technol 2019;29:289–95. https://doi.org/10.1016/j.ijmst.2018.08.011.
[9] Ran J, Qiu X, Hu Z, Liu Q, Song B, Yao Y. Enhance flotation separation of arsenopyrite and pyrite by low-temperature oxygen plasma surface modification. Appl Surf Sci 2019;480:1136–46. https://doi.org/10.1016/j.apsusc.2019.02.172.
[10] Zhang G, He Y, Wang H, Feng Y, Xie W, Zhu X. Removal of organics by pyrolysis for enhancing liberation and flotation behavior of electrode materials derived from spent lithium-ion batteries. ACS Sustainable Chem Eng 2020;8:2205–14. https://doi.org/10.1021/acssuschemeng.9b05896.
[11] Chen X, Kang D, Cao L, Li J, Zhou T, Ma H. Separation and recovery of valuable metals from spent lithium ion batteries: simultaneous recovery of Li and Co in a single step. Sep Purif Technol 2019;210:690–7. https://doi.org/10.1016/j.seppur.2018.08.072.
[12] Vanderbruggen A, Gugala E, Blannin R, Bachmann K, Serna-Guerrero R, Rudolph M. Automated mineralogy as a novel approach for the compositional and textural characterization of spent lithium-ion batteries. Miner Eng 2021;169:106924. https://doi.org/10.1016/j.mineng.2021.106924.
[13] Zhang T, He Y, Wang F, Li H, Duan C, Wu C. Surface analysis of cobalt-enriched crushed products of spent lithium-ion batteries by X-ray photoelectron spectroscopy. Sep Purif Technol 2014;138:21–7. https://doi.org/10.1016/j.seppur.2014.09.033.
[14] Yu J, He Y, Qu L, Yang J, Xie W, Zhu X. Exploring the critical role of grinding modification on the flotation recovery of electrode materials from spent lithium ion batteries. J Clean Prod 2020;274:123066. https://doi.org/10.1016/j.jclepro.2020.123066.
[15] Wang F, Zhang T, He Y, Zhao Y, Wang S, Zhang G, Zhang Y, Feng Y. Recovery of valuable materials from spent lithium-ion batteries by mechanical separation and thermal treatment. J Clean Prod 2018;185:646–52. https://doi.org/10.1016/j.jclepro.2018.03.069.
[16] He Y, Zhang T, Wang F, Zhang G, Zhang W, Wang J. Recovery of $LiCoO_2$ and graphite from spent lithium-ion batteries by Fenton reagent-assisted flotation. J Clean Prod 2017;143:319–25. https://doi.org/10.1016/j.jclepro.2016.12.106.
[17] Liu J, Wang H, Hu T, Bai X, Wang S, Xie W, Hao J, He Y. Recovery of $LiCoO_2$ and graphite from spent lithium-ion batteries by cryogenic grinding and froth flotation. Miner Eng 2020;148:106223. https://doi.org/10.1016/j.mineng.2020.106223.
[18] Shin H, Zhan R, Dhindsa KS, Pan L, Han T. Electrochemical performance of recycled cathode active materials using froth flotation-based separation process. J Electrochem Soc 2020;167:020504. https://doi.org/10.1149/1945-7111/ab6280.
[19] Zhan R, Oldenburg Z, Pan L. Recovery of active cathode materials from lithium-ion batteries using froth flotation. SMT Trends 2018;17:e00062. https://doi.org/10.1016/j.susmat.2018.e00062.
[20] Kim Y, Matsuda M, Shibayama A, Fujita T. Recovery of $LiCoO_2$ from wasted lithium ion batteries by using mineral processing technology. Resour Process 2004;51:3–7. https://doi.org/10.4144/rpsj.51.3.
[21] Zhan R, Yang Z, Bloom I, Pan L. Significance of a solid electrolyte interphase on separation of anode and cathode materials from spent Li-ion batteries by froth flotation. ACS Sustainable Chem Eng 2021;9:531–40. https://doi.org/10.1021/acssuschemeng.0c07965.
[22] Guangwen Z, Liu Z, Yuan X, He Y, Wei N, Wang H, Zhang B. Recycling of valuable metals from spent cathode material by organic pyrolysis combined with in-situ thermal reduction. J Hazard Mater 2022;430:128374. https://doi.org/10.1016/j.jhazmat.2022.128374.
[23] Vanderbruggen A, Salces A, Ferreira A, Rudolph M, Serna-Guerrero R. Improving separation efficiency in end-of-life lithium-ion batteries flotation using attrition pre-treatment. Minerals 2022;12:72. https://doi.org/10.3390/min12010072.
[24] Fan M, Tao D, Zhao Y, Honaker R. Effect of nanobubbles on the flotation of different sizes of coal particle. MINING METALL EXPLOR 2013;30:157–61. https://doi.org/10.1007/BF03402262.
[25] Zhou W, Niu J, Xiao W, Ou L. Adsorption of bulk nanobubbles on the chemically surface-modified muscovite minerals. Ultrason Sonochem 2019;51:31–9. https://doi.org/10.1016/j.ultsonch.2018.10.021.

[26] Rulyov NN, Sadovskiy DY, Rulyova NA, Filippov LO. Column flotation of fine glass beads enhanced by their prior heteroaggregation with microbubbles. Colloids Surf A Physicochem Eng Asp 2021;617:126398. https://doi.org/10.1016/j.colsurfa.2021.126398.
[27] Nazari S, Shafaei SZ, Gharabaghi M, Ahmadi R, Shahbazi B. New approach to quartz coarse particles flotation using nanobubbles, with emphasis on the bubble size distribution. Int J Nanosci 2020;19:1850048. https://doi.org/10.1142/S0219581X18500485.
[28] Nazari S, Hassanzadeh A. The effect of reagent type on generating bulk sub-micron (nano) bubbles and flotation kinetics of coarse-sized quartz particles. Powder Technol 2020;374:160–71. https://doi.org/10.1016/j.powtec.2020.07.049.
[29] Zhou W, Ou L, Shi Q, Feng Q, Chen H. Different flotation performance of ultrafine scheelite under two hydrodynamic cavitation modes. Minerals 2018;8:264. https://doi.org/10.3390/min8070264.
[30] Pourkarimi Z, Rezai B, Noaparast M. Nanobubbles effect on the mechanical flotation of phosphate ore fine particles. Physicochem. Probl. Miner. Process. 2017;54:278–92. https://doi.org/10.5277/ppmp1804.
[31] Nazari S, Zhou S, Hassanzadeh A, Li J, He Y, Bu X, Kowalczuk PB. Influence of operating parameters on nanobubble-assisted flotation of graphite. J Mater Res Technol 2022;20:3891–904. https://doi.org/10.1016/j.jmrt.2022.08.137.
[32] Tussupbayev NK, Rulyov NN, Kravtchenco OV. Microbubble augmented flotation of ultrafine chalcopyrite from quartz mixtures. Miner Process Extr Metall (IMM Trans Sect C) 2016;125:5–9. https://doi.org/10.1179/1743285515Y.0000000014.
[33] Nazari S, Hassanzadeh A, He Y, Khoshdast H, Kowalczuk PB. Recent developments in generation, detection and application of nanobubbles in flotation. Minerals 2022;12:462. https://doi.org/10.3390/min12040462.
[34] Nazari S, Shafaei SZ, Hassanzadeh A, Azizi A, Gharabaghi M, Ahmadi R, Shahbazi B. Study of effective parameters on generating submicron (nano)-bubbles using the hydrodynamic cavitation. Physicochem. Probl. Miner. Process. 2020;56:884–904. https://doi.org/10.37190/ppmp/126628.
[35] Farrokhpay S, Filippova I, Filippov L, Picarraa A, Rulyov N, Fornasieroc D. Flotation of fine particles in the presence of combined microbubbles and conventional bubbles. Miner Eng 2020;155:106439. https://doi.org/10.1016/j.mineng.2020.106439.
[36] Sobhy A, Tao D. Nanobubble column flotation of fine coal particles and associated fundamentals. Int J Miner Process 2013;124:109–16. https://doi.org/10.1016/j.minpro.2013.04.016.
[37] Zhou ZA, Xu Z, Finch JA, Hu H, Rao SR. Role of hydrodynamic cavitation in fine particle flotation. Int J Miner Process 1997;51:139–49. https://doi.org/10.1016/S0301-7516(97)00026-4.
[38] Ahmadi R, Khodadadi Darban A, Abdollahy M, Fan M. Nano-microbubble flotation of fine and ultrafine chalcopyrite particles. Int J Min Sci Technol 2014;24:559–66. https://doi.org/10.1016/j.ijmst.2014.05.021.
[39] Weber ME, Paddock D. Interceptional and gravitational collision efficiencies for single collectors at intermediate Reynolds numbers. J Colloid Interface Sci 1983;94:328–35. https://doi.org/10.1016/0021-9797(83)90270-9.
[40] Ma F, Tao D, Tao Y, Liu S. An innovative flake graphite upgrading process based on HPGR, stirred grinding mill, and nanobubble column flotation. Int J Min Sci Technol 2021;31:1063–74. https://doi.org/10.1016/j.ijmst.2021.06.005.
[41] Tang C, Ma F, Wu T, Di Z, Ye W, Li M, Li X, Liu X. Study on surface physical and chemical mechanism of nanobubble enhanced flotation of fine graphite. J Ind Eng Chem 2023. https://doi.org/10.1016/j.jiec.2023.02.039.
[42] Calgaroto S, Azevedo A, Rubio J. Flotation of quartz particles assisted by nanobubbles. Int J Miner Process 2015;137:64–70. https://doi.org/10.1080/19392699.2019.1692340.
[43] Ma F, Tao D, Tao Y. Effects of nanobubbles in column flotation of Chinese sub-bi tuminous coal. Int. J. Coal Prep. Util. 2022;42:1126–42.
[44] Zhou S, Li Y, Nazari S, Bu X, Hassanzadeh A, Ni C, He Y, Xie G. An Assessment of the role of combined bulk micro- and nano-bubbles in quartz flotation. Minerals 2022;12:944. https://doi.org/10.3390/min12080944.
[45] Liu M, Peng Q, Luo B, Zhou C. The improvement of mechanical performance and water-response of carboxylated SBR by chitin nanocrystals. Eur Polym J 2015;68:190–206. https://doi.org/10.1016/j.eurpolymj.2015.04.035.
[46] Xia Y, Rong G, Xing Y, Gui X. Synergistic adsorption of polar and nonpolar reagents on oxygen-containing graphite surfaces: implications for low-rank coal flotation. J Colloid Interface Sci 2019;557:276–81. https://doi.org/10.1016/j.jcis.2019.09.025.
[47] Biswal BK, Jadhav UU, Madhaiyan M, Ji L, Yang E, Cao B. Biological leaching and chemical precipitation methods for recovery of Co and Li from spent lithium-ion batteries. ACS Sustainable Chem Eng 2018;6:12343–52. https://doi.org/10.1021/acssuschemeng.8b02810.
[48] Uddin S, Jin L, Mirnezami M, Finch JA. An apparatus to measure electrical charge of bubble swarms. J Colloid Interface Sci 2013;389:298–305. https://doi.org/10.1016/j.jcis.2012.08.056.
[49] Awad AS. Determination of mass loss rate and smoke generated of Jordanian hardwood timber under different flaming combustion and limited ventilation environment. WSEAS Trans Appl Theor Mech 2020;15:82–97. https://doi.org/10.37394/232011.2020.15.11.
[50] An H, Liu G, Craig VSJ. Wetting of nanophases: nanobubbles, nanodroplets and micropancakes on hydrophobic surfaces. Adv Colloid Interface Sci 2015;222:9–17. https://doi.org/10.1016/j.cis.2014.07.008.
[51] Zhang Z, Ren L, Zhang Y. Role of nanobubbles in the flotation of fine rutile particles. Miner Eng 2021;172:107140. https://doi.org/10.1016/j.mineng.2021.107140.
[52] Wang Y, Luo X, Qin W, Jiao F. New insights into the contact angle and formation process of nanobubbles based on line tension and pinning. Appl Surf Sci 2019;481:1585–94. https://doi.org/10.1016/j.apsusc.2019.01.292.
[53] Ishida N, Inoue T, Miyahara M, Higashitani K. Nano bubbles on a hydrophobic surface in water observed by tapping-mode atomic force microscopy. Langmuir 2000;16:6377–80. https://doi.org/10.1021/la000219r.
[54] Hampton MA, Nguyen AV. Nanobubbles and the nanobubble bridging capillary force. Adv Colloid Interface Sci 2010;154:30–55. https://doi.org/10.1016/j.cis.2010.01.006.
[55] Ding S, Xing Y, Zheng X, Zhang Y, Cao Y, Gui X. New insights into the role of surface nanobubbles in bubble-particle detachment. Langmuir 2020;36:4339–46. https://doi.org/10.1021/acs.langmuir.0c00359.
[56] Gu G, Sanders RS, Nandakumar K, Xu Z, Masliyah JH. A novel experimental technique to study single bubble–bitumen attachment in flotation. Int J Miner Process 2004;74:15–29. https://doi.org/10.1016/j.minpro.2003.08.002.
[57] Fan M, Tao D, Honaker R, Luo Z. Nanobubble generation and its applications in froth flotation (part II): fundamental study and theoretical analysis. Min Sci Technol 2010;20:159–77. https://doi.org/10.1016/S1674-5264(09)60179-4.

[58] Li H, Afacan A, Liu Q, Xu Z. Study interactions between fine particles and micron size bubbles generated by hydrodynamic cavitation. Miner Eng 2015;84:106–15.
[59] Ishida N, Kusaka Y, Ushijima H. Hydrophobic attraction between silanated silica surfaces in the absence of bridging bubbles. Langmuir 2012;28:13952–9. https://doi.org/10.1021/la303037d.
[60] Wu C, Nesset K, Masliyah J, Xu Z. Generation and characterization of submicron size bubbles. Adv Colloid Interface Sci 2012;179–182:123–32. https://doi.org/10.1016/j.cis.2012.06.012.
[61] Nazari S, Chehreh Chelgani S, Shafaei SZ, Shahbazi B, Matin SS, Gharabaghi M. Flotation of coarse particles by hydrodynamic cavitation generated in the presence of conventional reagents. Sep Purif Technol 2019;220:61–8. https://doi.org/10.1016/j.seppur.2019.03.033.
[62] Weijs JH, Lohse D. Why surface nanobubbles live for hours. Phys Rev Lett 2013;110:054501. https://doi.org/10.1103/PhysRevLett.110.054501.
[63] Stocco A, Möhwald H. The influence of long-range surface forces on the contact angle of nanometric droplets and bubbles. Langmuir 2015;31:11835–41. https://doi.org/10.1021/acs.langmuir.5b02922.
[64] Nishiyama T, Yamada Y, Ikuta T, Takahashi K, Takata Y. Metastable nanobubbles at the solid–liquid interface due to contact angle hysteresis. Langmuir 2015;31:982–6. https://doi.org/10.1021/la5036322.